

Contents lists available at ScienceDirect

Carbon

journal homepage: www.elsevier.com/locate/carbon



Porous carbon fibers from gel-spun polyacrylonitrile and poly(methyl methacrylate)-block-poly(acrylonitrile)



Jyotsna Ramachandran ^{d, 1}, Joel M. Serrano ^{a, 1}, Tianyu Liu ^a, Jinwon Cho ^d, Pedro J. Arias-Monje ^d, Mingxuan Lu ^e, Mohammad Hamza Kirmani ^d, John Elliott ^a, Seung Soon Jang ^d, Guoliang Liu ^{a, c, b, **}, Satish Kumar ^{d, *}

- ^a Department of Chemistry, Virginia Tech, 800 West Campus Drive, Blacksburg, VA, 24061, USA
- ^b Macromolecules Innovation Institute, Virginia Tech, 800 West Campus Drive, Blacksburg, VA, 24061, USA
- ^c Division of Nanoscience, Academy of Integrated Science, Virginia Tech, 800 West Campus Drive, Blacksburg, VA, 24061, USA
- ^d School of Materials Science and Engineering, Georgia Institute of Technology, Atlanta, GA, 30332, USA
- ^e School of Chemical and Biomolecular Engineering, Georgia Institute of Technology, Atlanta, GA, 30332, USA

ARTICLE INFO

Article history: Received 9 September 2021 Received in revised form 29 January 2022 Accepted 18 February 2022 Available online 26 February 2022

Keywords: Block copolymers Carbon fibers Electrochemical Mechanical Computational Energy storage

ABSTRACT

Block copolymer (BCP)-based porous carbon fibers represent an emerging structural and functional material for mechanical reinforcement and electrochemical energy storage. Herein, by gel-spinning polymer precursors of poly(acrylonitrile) (PAN) and poly(methyl methacrylate)-block-poly(acrylonitrile) (PMMA-b-PAN), we have produced a series of carbon fibers and systematically studied the morphological, mechanical, and electrochemical properties. Porous carbon fibers with BCP in the sheath exhibit a tensile strength of 1.1 GPa, tensile modulus of ~190 GPa, and electrochemical capacitance of 11 F g⁻¹ at 10 mV s⁻¹ when pyrolyzed at 1315 °C under tension. Without tension and at a pyrolysis temperature of 800 °C, the fibers with BCP as both the sheath and core components achieve the highest electrochemical capacitance of 70 F g⁻¹ at 10 mV s⁻¹. The characteristic correlation length of PMMA-b-PAN calculated through thermodynamically governed computational method, provides an estimate of pore size in the carbon fibers. Pore generation and their size in the carbon fibers were driven by kinetic processing parameters, in addition to the thermodynamic phase separation. This study shows that gelspinning of bicomponent PAN/PMMA-b-PAN fibers provide a versatile means for tuning the mechanical and electrochemical properties of porous carbon fibers, thus allowing for their potential use as structural energy storage materials.

© 2022 Elsevier Ltd. All rights reserved.

1. Introduction

Advances in energy storage have paved ways for multifunctional materials that possess both high energy density and load-bearing capacities, thus giving rise to a new class of high-performance structural energy storage materials [1]. The dual performance requirements of high energy storage capacity and mechanical strength limit the candidates available. For example, non-porous

carbon fibers are excellent structural materials owing to their superior mechanical properties (*e.g.*, strength to weight ratio) [2,3], but because of small surface areas, their electrochemical energy storage capacitance remains unsuitable for use in structural energy storage devices [1,4,5]. Exploiting their load-bearing capacity and improving their electrochemical energy storage performance are being actively pursued [6–11]. Imparting porosity to the carbon fibers has been considered a potential avenue to design structural energy storage materials. The introduction of pores improves the electrochemical energy storage performance, but it inevitably reduces the mechanical strength when compared to non-porous carbon fibers [12].

Tuning porosity to enhance the electrochemical performance of carbon fibers has been achieved through electrospinning a carbon precursor of poly(acrylonitrile) (PAN) blended with sacrificial

^{*} Corresponding author. School of Materials Science and Engineering, Georgia Institute of Technology, Atlanta, GA, 30332, USA.

^{**} Corresponding author. Department of Chemistry, Virginia Tech, 800 West Campus Drive, Blacksburg, VA, 24061, USA.

E-mail addresses: gliu1@vt.edu (G. Liu), satish.kumar@mse.gatech.edu (S. Kumar).

¹ These authors contributed equally to this work.

polymers such as poly(methyl methacrylate) (PMMA) and poly(styrene) (PS) [13,14]. By using block copolymers (BCP) of PMMA-b-PAN instead of polymer blends, Zhou et al. reported porous carbon fibers with uniform mesopores showing an ultrahigh surface-areanormalized capacitance of 66 μ F cm $^{-2}$ [15]. The tunability of BCP molecular weight, composition, and processing conditions provides additional mechanisms for controlling physical and electrochemical properties of porous carbon fibers [16–18]. Despite the excellent electrochemical energy storage performance, the mechanical properties of these fibers remain elusive. There are likely tradeoffs in the design of structural energy storage materials [4].

Much of the research into multifunctional porous carbon fibers have been conducted by electrospinning [15–18]. Gel-spinning, as opposed to electrospinning, provides a favorable route to obtain high strength and high modulus carbon fibers from PAN [19]. Hollow carbon fibers with a density of $\sim 1.15 \,\mathrm{g \ cm^{-3}}$, tensile strength of 2.3-3.0 GPa, and tensile modulus of 202-234 GPa were previously obtained from gel-spun bicomponent polymer fibers containing PAN in the sheath and sacrificial PMMA in the core, producing lightweight yet strong structural reinforcements [20–22]. The improved tensile moduli of these hollow carbon fibers were attributed to an enhanced graphitic order despite a low density. However, the potential of gel-spun fibers to serve as energy storage material was unaddressed. Carbon fibers with spherical, elongated and channel-like pores were gel spun from blends of PAN and sacrificial polymers including, poly(acrylic acid) (PAA), PMMA and poly(styrene-co-acrylonitrile) (SAN), respectively [23]. Porous carbon fibers from these gel-spun blends had 15-40% higher specific tensile modulus than the non-porous PAN based fibers. Nevertheless, the electrochemical performance of these fibers was not characterized.

Herein, we studied the preparation of porous carbon fibers from gel-spun BCP fibers and their use as structural energy storage materials. To mitigate the effect of porosity on the structural properties [5,24], we designed bicomponent fibers of BCP with a reinforcing high-molecular weight PAN. BCP enhanced the electrochemical performance owing to the development of mesopores from the sacrificial block, meanwhile PAN balanced the loss in mechanical properties through graphitic ordering during pyrolysis. The polymer fibers were subjected to varying stabilization and carbonization processes, allowing for investigation of the effects of processing conditions on the mechanical and electrochemical performance of the porous carbon fibers. Through structural, mechanical, and electrochemical characterizations, we elucidated the tradeoff between structural support and electrochemical energy storage performance of the porous carbon fibers.

2. Experimental

2.1. Materials

Poly(acrylonitrile-co-methacrylic acid) (PAN; viscosity average molecular weight, M_v , 500 kDa) was obtained from Japan Exlan, Co. Acrylonitrile (AN, \geq 99%), methyl methacrylate (MMA, \geq 99%), azobisisobutyronitrile (AIBN, \geq 98%), benzene (\geq 99.9%), aluminum oxide (activated, neutral, Brockmann Activity I), N_i -dimethylformamide (DMF, \geq 99.7%), and dimethyl sulfoxide (DMSO, \geq 99.9%) were obtained from Sigma-Aldrich. The chain transfer agent cumyl dithiobenzoate (CBD) was synthesized similar to that in a previous report [25]. Methanol was used for polymer coagulation and washing. Nickel foam was purchased from MTI (surface density = 350 g m $^{-2}$) and used as electrode substrates. AN and MMA monomers were passed through neutral alumina columns to remove inhibitors prior to use. All other chemicals were used as received without further modifications.

2.2. Synthesis of PMMA-b-PAN

Poly(methyl methacrylate)-block-poly(acrylonitrile) (PMMA-b-PAN) was synthesized via reversible addition-fragmentation chain transfer (RAFT) polymerization. First, a mixture of MMA (65.0 mL, 309 mmol), CDB (169 mg, 0.309 mmol), and AIBN (50.8 mg, 0.155 mmol) were dissolved in benzene (103 mL) in a 1-L Schlenk flask. The mixture was subjected to three cycles of freeze-pumpthaw (FPT) followed by back-filling with N2 to remove any residual oxygen. The flask was placed in an oil bath at 60 °C for 20 h to synthesize PMMA macro-chain transfer agents (CTAs) with a number average molecular weight (M_n) of 60 kDa. The resulting PMMA macro-CTAs were precipitated in methanol, filtered twice, and dried under vacuum for 12 h. The purified PMMA macro-CTA was used to synthesize PMMA-b-PAN. PMMA macro-CTA (2.60 g, 10.8 μmol), AN (10.4 mL, 43.3 mmol), AIBN (1.78 mg, 2.70 μmol), and DMSO (28.9 mL) were mixed in a 1-L Schlenk flask. The mixture was degassed by three FPT cycles and then heated in an oil bath at 65 °C under N₂ atmosphere. After 24 h of reaction, the BCP contained a PAN block with a M_n of 100 kDa (Table 1). The resulting PMMA-b-PAN block copolymers were purified following the same procedures as PMMA macro-CTAs.

2.3. Polymer characterizations

Using size exclusion chromatography (SEC), number-average molecular weight (M_n) and polydispersity index (PDI) were measured on an EcoSEC HLC-8320GPC equipped with a DynaPro Nanostar photometer and light scattering detector. The mobile phase was DMF containing 0.05 M LiBr. The eluent flow rate was 0.5 mL min⁻¹ with a column temperature of 50 °C. Each SEC trace consumed 100 μ L of 1 mg mL⁻¹ polymer solution.

2.4. Gel spinning of polymer fibers

To prepare spinning solutions, PAN (11.5 g) was dissolved in prechilled DMF (0 °C, 100 mL) and then heated to 70 °C for 3 h using a silicone oil bath. Separately, PMMA-b-PAN (20 g) was added to DMF (100 mL) at room temperature, then heated at 50 °C for 1 h using a silicone oil bath and finally at 70 °C for 3 h. The polymer fibers were gel-spun using a spinning equipment manufactured by Hills, Inc., which has two barrel-shaped reservoirs for co-extruding bicomponent fibers from two solutions (schematic reported in Ref. [26]). The core and sheath spinning solutions were extruded through a single hole spinneret (diameter, 200 µm). The area ratio of the core and sheath components was adjusted by varying the flow rates of the two solutions (Table 2). The extrudate was passed through an air gap of 6 cm and then through a methanol coagulation bath at -50 °C. The as-spun fibers were collected on the takeup-roller and stored in methanol overnight. The fibers were subsequently drawn at room temperature and then passed through a glycerol bath at 160 °C. Draw ratio (DR) of the fibers is defined as the ratio of the collection speed at the take-up rollers to the feed

Table 1 Polymer characteristics of synthesized PMMA-*b*-PAN.

	PMMA-b-PAN (BCP)	
	PMMA	PAN
Molecular Weight ^a (Da)	60,000	100,000
Weight Ratio Total Molecular Weight ^a (Da)	0.38 160,000	0.62
PDI	1.19	

^a Based on number-average molecular weight as determined by SEC using a light-scattering detector.

Table 2Configurations of gel-spun polymer fibers.

Designation	Core (A1)	Sheath (A2)	Area Ratio (A1:A2)	Overall PMMA content (wt.%) ^a
'BCP sheath'	PAN	PMMA-b-PAN	70:30	11
'BCP core'	PMMA-b-PAN	PAN	30:70	11
'BCP both'	PMMA-b-PAN	PMMA-b-PAN	_	38
'PAN both'	PAN	PAN	_	0

^a For 'BCP both' fibers, the weight fraction of PMMA in the PMMA-b-PAN is 38 wt.%, as obtained from Table .1. For the 'BCP sheath' and 'BCP core' fibers, the area of PMMA-b-PAN is 30%. Using the relationship of Area % \approx Volume % \approx Weight % ($_{\rho PAN} \approx _{\rho PMMA} = 1.18 \text{ g cm}^{-3}$), the weight fraction of PMMA in the 'BCP sheath' or 'BCP core' fibers is calculated to be 11%.

speed. Fibers were assigned draw ratios at the stages of spinning (SDR), room temperature (RDR) and hot drawing (HDR) due to the difference of the feed and collection speeds. The total draw ratio (TDR) was then calculated as the product of the draw ratios at the three stages: SDR*RDR*HDR. For comparison, single component PAN fibers with total draw ratio (TDR) of 22 were also produced following the same protocol and similar processing parameters. Table 3 lists the processing parameters of the two solutions used for spinning bicomponent and single component fibers during the study.

2.5. Stabilization and carbonization of polymer fibers without tension

Without tension throughout the process, the polymer fibers were first stabilized in air at 280 °C for 8 h (heating rate, 1 °C min $^{-1}$) in an electrical tube furnace (Model STF55433C-1, Lindberg/Blue M). Subsequently, the fibers were pyrolyzed at 800 °C for 1 h (heating rate, 10 °C min $^{-1}$) in a constant N_2 flow of 200 standard cubic centimeters per minute (sccm) under 1 atm.

2.6. Stabilization and carbonization of polymer fibers with tension

For comparison, another two groups of polymer fibers were stabilized and carbonized under tension in a tube furnace (Model H17HT2.5x24, Micropyretics Heaters International, Inc). The two groups of polymer fibers underwent two different thermal stabilization protocols (in air) before carbonization: one-step stabilization and two step-stabilization. In the first group, polymer fibers were heated from room temperature to 280 °C (heating rate, 3 °C min⁻¹) for 180 min, under a stress of 5-10 MPa, in air. The stabilized fibers were carbonized under N₂ atmosphere at 800 °C (heating rate, 10 °C min^{-1}) for 60 min under a constant stress of 5–10 MPa. The stress was based on the force over the overall cross-sectional area of the polymer fibers. In the second group, polymer fibers were stabilized at 265 °C for 170 min (heating rate, 3 °C min⁻¹) and 305 °C for 10 min (heating rate, 3 °C min⁻¹) in air and under constant stress of 10 MPa. The stabilized fibers were carbonized under N₂ by heating from room temperature to 1315 °C (heating rate, 5 °C min⁻¹) for 10 min, under a constant stress of 5-10 MPa.

Table 3Parameters of the PMMA-*b*-PAN and PAN solutions used for spinning polymer fibers in all three different configurations.

	PMMA-b-PAN	PAN
Solid Content (g dL ⁻¹) ^a	20	11.5
Solvent	DMF	
Spinning Barrel Temperature (°C)	70	
Spinneret Temperature (°C)	80	
Coagulation Bath	Methanol (-50 °C)	

^a Solid content of the spinning solution is the weight of polymer dissolved in a given volume of solvent (DMF).

2.7. Morphological characterizations

Morphologies of the fibers were characterized on two fieldemission scanning electron microscopes (FE-SEM): one at Virginia Tech (LEO 1550) with an accelerating voltage of 2 kV and a working distance of ~3 mm and the other at Georgia Tech (HITACHI SU8230) with an accelerating voltage of 1–5 kV and a working distance of ~5–7 mm. *ImageJ* software was used to analyze the SEM images and measure the average pore size of the carbon fibers.

2.8. Physical characterizations

Thermal gravimetrical analysis (TGA) was performed on a Discovery TGA5500 (TA instruments) analyzer by heating samples from room temperature to 700 °C at a ramp rate of 10 °C min⁻¹ under ultrapure N₂ (flow rate: 25 mL min⁻¹). N₂ and CO₂ physisorption was conducted by a pore analyser (3Flex Pore Analyzer, Micromeritics Instrument Corp.) at 77 K and 273 K, respectively. Prior to physisorption, all carbon fibers were heated at 90 °C for 60 min and then at 350 °C for 900 min in N₂ to desorb any moisture and hydrocarbons. The ramp rates of both heating processes were 10 °C min⁻¹. The surface areas were calculated using Brunauer-Emmett-Teller (BET) theory, and the pore size distributions were derived from non-local density functional theory (NLDFT) [15].

2.9. Mechanical and structural characterization

Rheology characterization of the spinning solution was performed on an ARES Rheometer with parallel plate geometry (25 mm plate diameter and 1 mm gap between the plates) at room temperature. A constant strain of 1% was applied and the angular frequency varied from 0.1 to 300 rad s^{-1} . Tensile testing of all the polymer fibers, except 'BCP sheath', was done using a single filament testing equipment (FAVIMAT⁺), at a strain rate of 1% s⁻¹ and gauge length of 25.4 mm. At least 25 samples were tested for each type of fiber. 'BCP sheath' fibers, due to the crimp, were tested using RSA III solids analyzer (Rheometric Scientific Co.), at a strain rate of 1% s⁻¹ and gauge length of 25.4 mm by mounting single filaments on paper tabs. Temperature-sweep dynamic mechanical analysis (DMA) was conducted on fiber bundles with an effective crosssectional area of 55 μm² at a frequency of 1 Hz and a heating rate of 1 °C min⁻¹ from 30 to 180 °C using RSA III solids analyzer. Single filament tensile testing of carbon fibers was done using RSA III solids analyzer at a strain rate of 0.1% s⁻¹ and gauge length of 12.7 mm by mounting single filaments on paper tabs. The tensile properties were calculated from stress-strain curves of the individual filaments based on the overall cross-sectional area. Wideangle X-ray diffractions (WAXD) patterns were obtained on a Rigaku MicroMax 002 X-ray generator (Cu Kα radiation, $\lambda = 1.5418$ Å, 50 kV and 0.6 mA) equipped with a R-axis IV++ detector. The crystal size of PAN was calculated from the full width at half-maximum intensity (FWHM) of its crystalline peak from the equatorial scan using Scherrer's equation with K (a dimensionless

shape factor constant) of 0.9.

2.10. Electrochemical characterizations

Electrochemical tests were performed on a PARSTAT 4000+ electrochemical workstation (Princeton Applied Research, AMETEK Inc.) with a three-electrode configuration. The working electrodes were made by ~1 mg of carbon fibers sandwiched between two pieces of nickel foam and pressed at 4 metric tons for 30 s with a benchtop hydraulic press (Stongway, Model 46269). An Ag/AgCl electrode (in saturated KCl aqueous solution) and a piece of nickel foam served as the reference and counter electrodes, respectively. The electrolyte was 3 M aqueous KOH solution. Cyclic voltammetry (CV) was carried out within a potential window from 0 to -0.8 V vs. Ag/AgCl. CV curves were collected at various scan rates between 10 and 1000 mV s⁻¹ and chronopotentiometry (CP) tests were performed at 10 A g⁻¹. The CV-based gravimetric capacitances were calculated using the following equation [27]:

$$C = \frac{1}{2(V_t - V_0)\nu} \int_{V_0}^{V_t} |I_m(V)| dV$$
 (1)

where $I_{\rm m}$ (V) is the current density (A g⁻¹); v is the scan rate (mV s⁻¹); V_0 and $V_{\rm t}$ are the lower and upper potential limits of the potential window, respectively. Alternatively, CP capacitance was calculated using the discharging time (Δt) [28]:

$$C = \frac{I_m \Delta t}{\Delta V} \tag{2}$$

where $I_{\rm m}$ is the current density (A g⁻¹) and ΔV is the potential window. Electrochemical impedance spectroscopy (EIS) was conducted between 0.1 and 100 kHz with 10 mV perturbation at open-circuit potentials. The spectra were fit according to an equivalent circuit using ZSimpWin software.

2.11. Calculation of interaction parameter and characteristic correlation length

Computational methods were used to calculate the interaction parameter and the characteristic correlation length of PMMA-b-PAN. The interaction parameter χ , defined by Flory-Huggins solution theory, is key for determining the miscibility between two or more polymers. In previous studies, we developed a computational method to estimate the χ -parameter, and the results were well-agreed with several experimental systems [29,27]. The χ -parameter defined on the basis of mixing energy is expressed as follows:

$$\chi_{i,j} = \frac{\Delta E_{ij}}{RT} \tag{3}$$

where $\chi_{i,j}$ is the χ -parameter between polymer i and j, which in this case are PMMA and PAN, respectively, and ΔE_{ij} is the mixing energy of polymer i and j (Computation C1).

Initially, the interaction parameters of low molecular weight PMMA-b-PAN (monomer, dimer, and trimer) with various molecular conformations were computed through multiscale models before extending the calculation to synthesized BCP with molecular weight of ~160 kDa. In this study, three different molecular conformations, namely syndiotactic (Syn), isotactic (Iso), and atactic (Ata) PMMA and PAN, were considered for the ΔE_{ij} calculations. Owing to the experimental conditions, both PMMA and PAN are likely to be randomly orientated in this study, and thus we calculated $\chi_{i,i}$ for PMMA Iso & PAN Syn and PMMA Syn & PAN Iso blocks

to mimic the atactic nature of both the polymers.

Based on the $\chi_{i,j}$ calculations results, we further carried out a dissipative particle dynamic (DPD; Computation C2) simulation to investigate the morphology of the synthesized PMMA-b-PAN by employing the equation from our previous work and then calculated the characteristic correlation length via radial distribution function (RDF) analysis [29,27]. The characteristic correlation length defines the scale of a phase separation which can be directly compared to X-ray diffraction data.

3. Results and discussion

The precursor to the carbon fibers, PMMA-b-PAN, was synthesized by RAFT polymerization with a $M_{\rm n}$ of 60-b-100 kDa, as characterized by SEC (Fig. S1). The molecular weight was sufficiently high for gel-spinning, but significantly lower than that of typical PAN ($M_{\rm v}=500$ kDa) for synthesizing carbon fiber with high tensile strength and modulus [19]. To achieve good mechanical properties, PAN was used along with BCP to prepare polymer fibers of four different configurations: 1) BCP in sheath and PAN in core ('BCP sheath'); 2) BCP in core and PAN in sheath ('BCP core'); 3) BCP in core and sheath ('BCP both'); and 4) PAN in core and sheath ('PAN both' as a control) (Table 2). The amount of PMMA in the 'BCP both' and bicomponent fibers ('BCP sheath' and 'BCP core') were 38 and 11 wt%, respectively.

3.1. Morphologies of carbon fibers

By varying the processing temperature and tension during pyrolysis, the polymer fibers were processed into porous carbon fibers with tunable mechanical and electrochemical properties. After pyrolysis at 800 °C without tension, the four types of carbon fibers showed different morphologies (Figs. 1-2). The average pore size of the fibers was calculated based on SEM images using an image processing software, ImageJ. When BCP was extruded in the sheath, the exterior showed axially aligned mesopores with an average pore size of 27 ± 8 nm. When BCP was extruded in the core, the PAN sheath formed a solid (i.e non-porous) carbon sheath and the BCP core yielded aligned mesopores with an average size of 30 \pm 9 nm. For 'BCP both' carbon fibers, both cross section and the fiber surface exhibited well distributed and aligned pores of 21 \pm 7 nm in size. The difference in the mesopore sizes in these three types of porous carbon fibers was not considered statistically significant, given the relatively large error bars. Regardless, the BCP-derived mesopores in all cases were elongated (non-spherical) and axially aligned, owing to the multi-stage drawing and shearing in the fiber preparation process. As a control, the 'PAN-both' fibers showed no mesopores.

The porous structure and surface area were further characterized by CO₂ and N₂ sorption [15,17]. CO₂ physisorption probes micropores (<2 nm) within the carbon fibers. For all three porous carbon fiber configurations, CO₂ sorption revealed type I isotherms and the hysteresis within the isotherms indicted the presence of micropores (Fig. 3a). The micropore size distribution for all the three porous fibers exhibited multiple distinct peaks centered at ~0.53, 0.86, and 1.29 nm (Fig. 3c). N₂ sorption showed type IV isotherm [30], for 'BCP both', 'BCP sheath', and 'BCP core' carbon fibers, with hysteresis at $0.7 < P/P_0 < 0.9$ indicating the presence of mesopores (Fig. 3b). Based on NLDFT, the mesopore volume decreased in the sequence of 'BCP both', 'BCP sheath', and 'BCP core' (Fig. 3c), with 'BCP both' showing a distinct peak at 23 nm. The same trend was reflected in the surface area of these fibers. 'BCP both' carbon fibers exhibited the highest surface area (264 m² g⁻¹) followed by 'BCP sheath' (27 m² g⁻¹) and 'BCP core' (2 m² g⁻¹) carbon fibers. 'BCP both' based carbon fibers possessed the highest

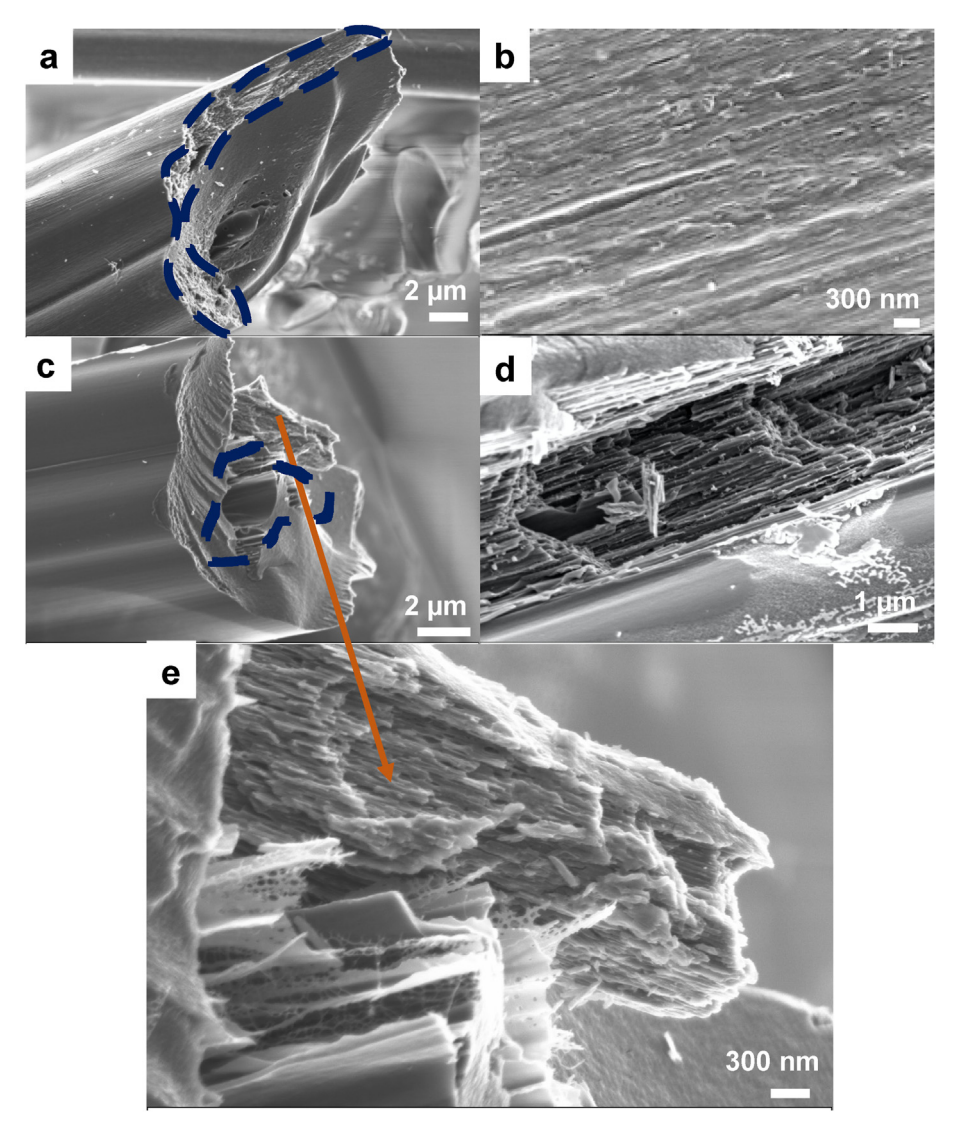


Fig. 1. Representative cross-sectional (a, c, d, and e) and fiber-surface (b) SEM images of carbon fibers from varying polymer fibers: (a-b) 'BCP sheath', (c-e) 'BCP core'. All carbon fibers were pyrolyzed without tension at 800 °C.

amount of PMMA (38 wt%) and in addition, the mesopores were present in both the sheath and core portions which contributed to these fibers having the highest mesopore volume and surface area. 'BCP sheath' carbon fibers had a larger mesopore volume and surface area than the 'BCP core' carbon fibers, despite the same amount of PMMA (11 wt%). This phenomenon might arise owing to the larger amount of PMMA derived pores along the surface of 'BCP sheath', thereby enhancing accessibility during physisorption. With BCP-derived mesopores in the sheath, the gas molecules could assess pores both near the surface and in the interior. However, with BCP-derived mesopores in the core, the PAN-derived non-porous carbon layer shielded the access to pores in the core, thereby reducing the effective mesopore volume and surface area of 'BCP core' fibers.

We also investigated morphologies of carbon fibers after pyrolysis under tension (Figs. 4–5, S3–S5). While axial alignment of mesopores was a consistent feature among all BCP-derived carbon fibers with or without tension, the mesopore size differed. As the pyrolysis temperature was increased from 800 to 1315 °C, the average mesopore size of 'BCP sheath' fibers marginally increased from 13 to 19 nm 'BCP core' fibers displayed solid carbonized

exteriors arising from the PAN sheath from both pyrolysis temperatures, 800 and 1315 $^{\circ}\text{C}.$

Based on the cross-sectional SEM images, we analyzed the morphology of the bicomponent fibers. Coaxial core-sheath (*C*/S) morphology was expected for the bicomponent fibers after gel spinning through a single spinneret (Figs. 6a and 6c), but interestingly the actual fibers showed different morphologies (Figs. 1a, 1c, 4a, and 5c). In the 'BCP sheath' fibers, the PAN core was not fully encompassed by the 'BCP sheath' and the latter was pushed to one side of the fibers, rendering a side-by-side (S/S) instead of C/S morphology (Figs. 1a, 4a and 6b). In 'BCP core' fibers, the core shifted away from the center but was still fully encompassed by the sheath (Figs. 1c, 5c and 6d). These morphologies persisted in carbon fibers after pyrolysis, with or without tension.

To coaxially spin a stable C/S morphology with the sheath fully encapsulating the core, viscosity of the sheath solution must be lower than that of the core solution since the sheath experiences higher shear force [31–33]. In gel-spinning 'BCP core' polymer fibers, the viscosity of the BCP solution (20 g dL $^{-1}$) was higher than that of the PAN solution (11.5 g dL $^{-1}$) (Fig. S6a), thus rendering a C/S morphology. Upon switching the two components to prepare 'BCP

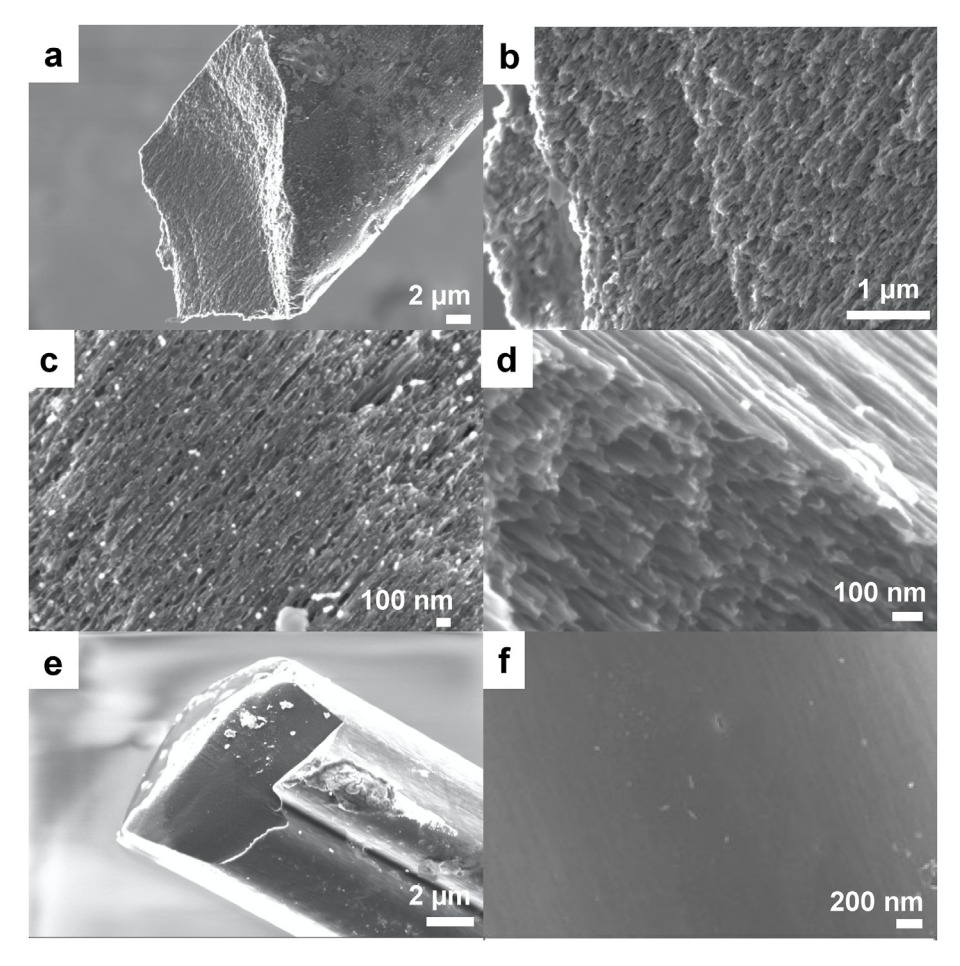


Fig. 2. Representative cross-sectional (a, b, d, and e) and fiber-surface (c and f) SEM images of carbon fibers from varying polymer fibers: (a-d) 'BCP both', and (e-f) 'PAN both'. All carbon fibers were pyrolyzed without tension at 800 °C.

sheath' polymer fibers, the lower viscosity of the PAN solution than that of BCP in the sheath solution drove the PAN from the core towards the edge to experience the higher shear force. Hence, BCP could not encapsulate PAN, leading to a S/S morphology.

3.2. Mechanical and structural characteristics of polymer fibers

Single component 'BCP both' and 'PAN both' polymer fibers showed different drawabilities of TDR = 13.2 and 22, respectively. Due to the S/S morphology and different drawabilities, BCP and PAN in 'BCP sheath' polymer fibers were drawn to different degrees, and thus 'BCP sheath' carbon fibers exhibited a crimped behavior. Crimp is prevalent in bicomponent fibers with the S/S morphology because the two components, if having differential characteristics like drawabilities and elasticity, are subjected to differential (imbalanced) force upon drawing [34–37]. Differently, in 'BCP core' polymer fibers that had a C/S morphology, the encapsulated BCP with lower drawability limited the drawability of the PAN sheath, resulting in the lowest TDR among the studied polymer fibers.

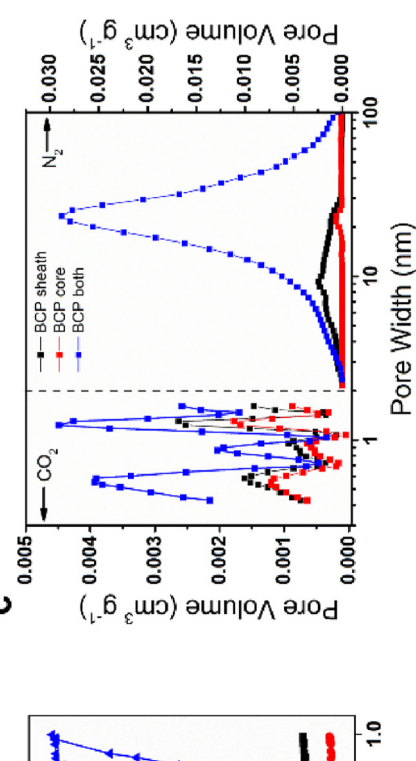
The mechanical properties of polymer fibers were influenced by the polymer constituents (BCP or PAN) and position of BCP (Table 4). Among the BCP-containing polymer fibers, 'BCP core' had the highest tensile strength and modulus, followed by 'BCP sheath' and 'BCP both'. Because BCP possessed a lower molecular weight (< PAN) and it contained PMMA [20,21], all three BCP-containing polymer fibers exhibited inferior tensile properties to 'PAN both', which had a substantially higher molecular weight PAN as both the

sheath and core components.

In a previous study, bicomponent PAN-carbon nanotubes (CNT) fibers with PAN (either in the sheath or core) as the reinforcement showed better tensile properties than single component PAN-CNT fibers [38]. In this study, the reinforcing effect of PAN was prevalent in the 'BCP core', which showed better tensile strength and modulus than 'BCP both' polymer fibers. Despite a higher draw ratio and reinforcing PAN core, the 'BCP sheath' polymer fibers showed mechanical properties inferior to 'BCP core' polymer fibers and similar to 'BCP both' polymer fibers. This was probably owing to the crimping effect arising from their S/S morphology, similar to previous reports [35,39].

Integrated WAXD graphs of the polymer fibers revealed peaks corresponding to the amount of PMMA in the fibers (Fig. 7). Due to the low PMMA content (11%), the bicomponent polymer fibers of 'BCP sheath' and 'BCP core' showed two peaks at ~17° and 30°, both characteristic of PAN. In contrast, with a PMMA content of 38%, 'BCP both' polymer fibers exhibited another peak at ~12°, representative of PMMA.

We further assessed the crystalline structures in 'BCP both', 'BCP sheath', 'BCP core', and 'PAN both' polymer fibers (Table 5). 'BCP both' polymer fibers showed the lowest crystallinity and crystal size due to the highest content of amorphous PMMA (38 wt%) and the absence of high molecular weight PAN. 'BCP core' polymer fibers exhibited the highest crystallinity and crystal size among the three BCP-containing systems, resulting in their highest tensile modulus of 16.8 GPa. Crimped 'BCP sheath' polymer fibers, despite



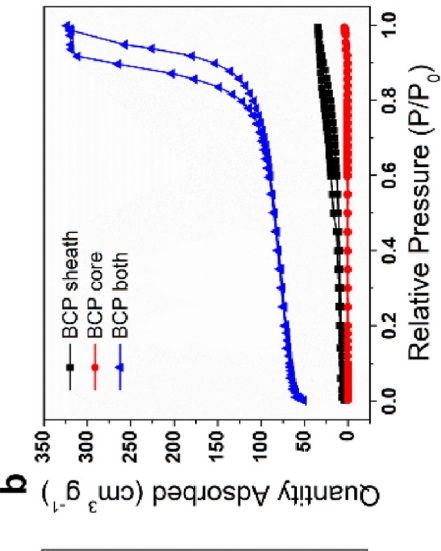
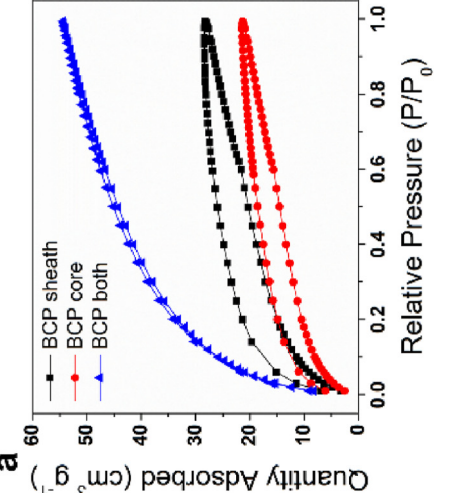


Fig. 3. Gas physisorption of carbon fibers after pyrolysis at 800 °C without tension: (a) CO₂-physisorption isotherms, (b) N₂-physisorption isotherms, and (c) pore width distributions based on NLDFT.



a higher draw ratio than 'BCP core' polymer fibers exhibited lower crystallinity, smaller crystal size, poorer crystal orientation, and thus lower mechanical properties. 'PAN both' fibers with the highest orientation exhibited the highest tensile strength and modulus than all the BCP-containing polymer fibers.

The amount of PMMA also influenced the packing of PAN crystals, as indicated by the d-spacing ratio determined from the peaks at ~17° and ~30° ($d_{17°}/d_{30}$ °). 'BCP sheath', 'BCP core' and 'PAN both' polymer fibers had ratios of 1.731, 1.731 and 1.734, respectively, all closer to the value of 1.732 for hexagonally packed PAN crystals [40]. The low content of PMMA (11 wt%) in these bicomponent polymer fibers was insufficient to substantially affect the PAN crystallization and packing, and thus they exhibited structural parameters characteristic of PAN (Fig. 7 and Table 5).

The dynamic mechanical behaviors including storage modulus and tan δ were studied as a function of temperature (Fig. 8). The storage moduli of 'BCP both', 'BCP sheath', and 'BCP core' polymer fibers decreased with temperature. 'BCP core' polymer fibers showed the highest moduli in the range of 30–180 °C. At room temperature, the storage modulus decreased in the order of 'BCP core' > 'BCP sheath' ~ 'BCP both', similar to their tensile moduli (Table 4).

PAN exhibits $\tan \delta$ peaks arising from thermo-mechanical transitions including: 1) α transition related to molecular motion in amorphous region (~140–160 °C) and 2) β_c transition corresponding to molecular motion in para-crystalline region of PAN (~75–110 °C) [41–44]. The glass transition temperature for PMMA is around 110–115 °C [45]. In this work, the bicomponent fibers revealed $\tan \delta$ peak at ~ 90 °C, which is attributed to the β_c relaxation of PAN. Contrastingly, the $\tan \delta$ peak of 'BCP both' polymer fibers showed at ~135 °C, which is attributed to two characteristics: 1) the increased glass transition temperature of PMMA due to an interfacial augment effect of block copolymers and 2) the α transitions of amorphous PAN with lower crystallinity [25]. In short, 'BCP both' polymer fibers showed thermomechanical behaviors characteristic of both PMMA and PAN, whereas 'BCP core' and 'BCP sheath' polymer fibers presented dominantly PAN characteristics.

3.3. Mechanical and structural properties of carbon fibers

Without tension, all polymer fibers were pyrolyzed successfully at 800 °C to produce carbon fibers. With tension, 'BCP both' polymer fibers broke after stabilization, and 'BCP sheath' and 'BCP core' polymer fibers were mechanically strong to survive the stabilization and carbonization at either 800 °C or 1315 °C to produce porous carbon fibers. The different mechanical strengths of these fibers are due to three reasons. First, unlike 'BCP core' and 'BCP sheath' polymer fibers, 'BCP both' polymer fibers lacked a high molecular weight PAN to reinforce the structure. Second, the dynamic storage modulus of 'BCP both' polymer fibers decreased rapidly with temperature (Fig. 8a), indicating a significant reduction in the mechanical integrity during thermal treatment. Third, due to the high PMMA content of 38 wt%, 'BCP both' polymer fibers would produce carbon fibers with a high degree of porosity, much higher than those of the 'BCP core' and 'BCP sheath' carbon fibers (Fig. 3c). Thus, a combination of low polymer molecular weight, reduced mechanical strength upon thermal treatment, and high porosity caused 'BCP both' fibers to fracture during stabilization.

We assessed the influence of pyrolysis temperature and BCP position on the mechanical properties of the bicomponent fibers pyrolyzed under tension. As expected, the mechanical properties of carbon fibers pyrolyzed at 1315 °C were higher than those at 800 °C (Table 6) [2,46]. Irrespective of BCP in the core or sheath, bicomponent 'BCP core' and 'BCP sheath' carbon fibers after pyrolysis at 1315 °C showed similar tensile strengths and tensile moduli

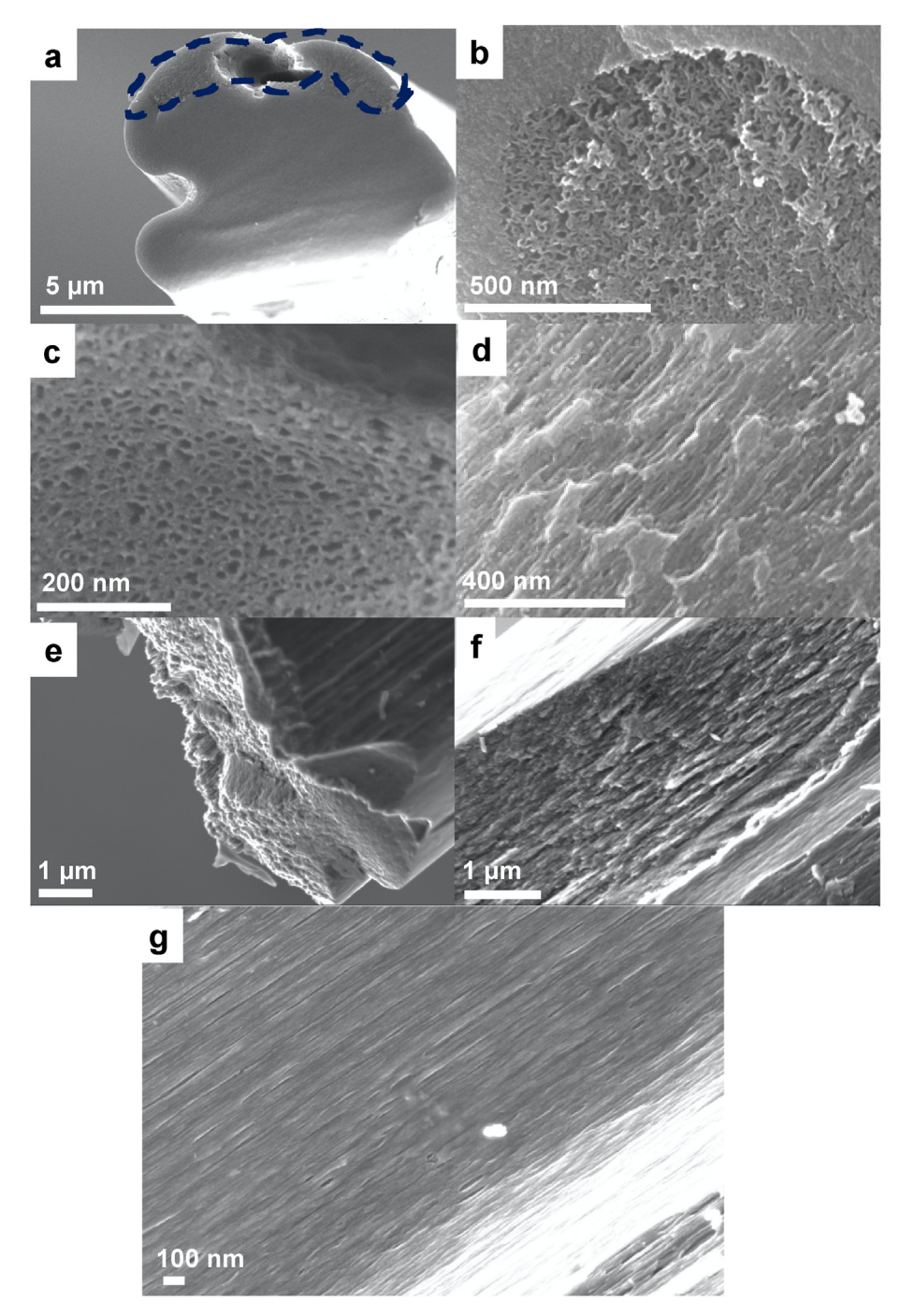


Fig. 4. Representative SEM images of carbon fibers after pyrolysis of 'BCP sheath' polymer fibers at (a-d) 800 °C and (e-g) 1315 °C under tension. Panels a, b, c, e, and f are cross-sections. Panels d and g are the fiber surfaces.

(Table 6). Their tensile strengths and moduli, however, were lower than those for the non-porous carbon fibers from PAN only (tensile strength of 2.08 GPa and tensile modulus of 288 GPa for PAN derived carbon fibers at 1315 °C) [26]. Similar to a previous report by Chen et al. [12], the modulus decreased due to the loss of load bearing area, and the tensile strength decreased due to the non-uniform stress concentration around pores. Owing to the 'crimping effect' and low pyrolysis temperature of 800 °C, 'BCP sheath' carbon fibers did not even withstand the sample preparation required for tensile testing.

In previous reports [4,12], porous carbon fibers from electrospun

PAN/PMMA blends had tensile modulus of ~70 GPa when pyrolyzed at 1100 °C. Notably, 'BCP core' carbon fibers from gel-spinning herein showed a similar tensile modulus of ~70 GPa at a lower pyrolysis temperature of 800 °C, and more than twice the modulus at 1315 °C [4,12]. Porous carbon fibers, carbonized at 1315 °C, from gel-spun blends of PAN-PMMA (~10 wt% PMMA) had tensile strength of ~1.5 GPa and tensile modulus of 281 GPa, closer to the non-porous PAN fibers [23]. Comparing the blends and BCP derived fiber, the significant difference lay in the molecular weights of PAN while the remaining factors including weight percent of PMMA (~11 wt%; Table 2) and pyrolysis conditions (1315 °C with tension)

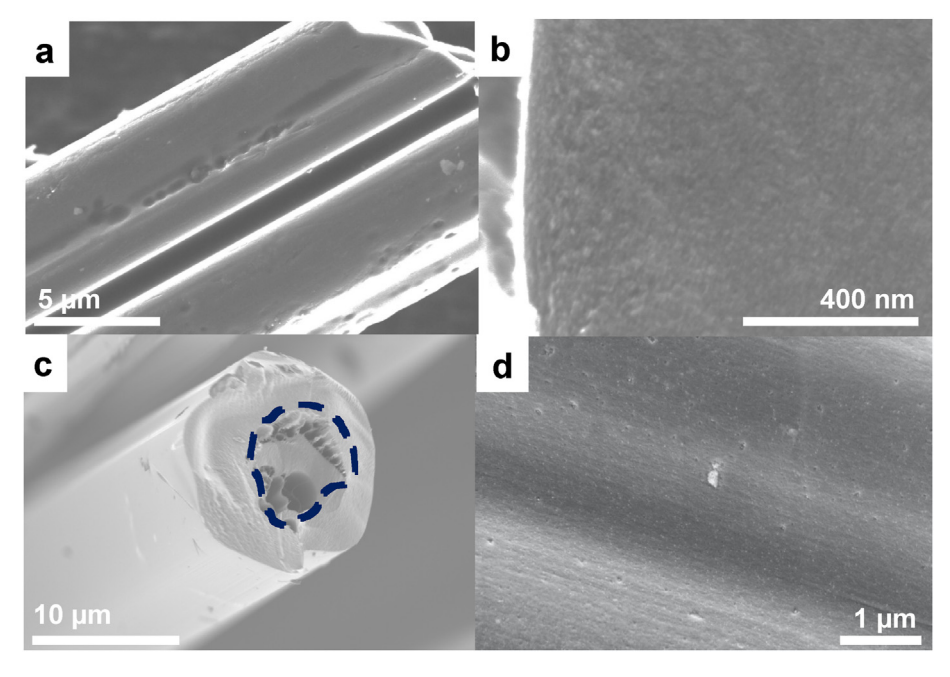


Fig. 5. Representative SEM images of carbon fibers after pyrolysis of 'BCP core' polymer fibers at (a and b) 800 °C and (c and d) 1315 °C under tension. Panels a and d are the fiber surfaces. Panels b and c are cross-sections.

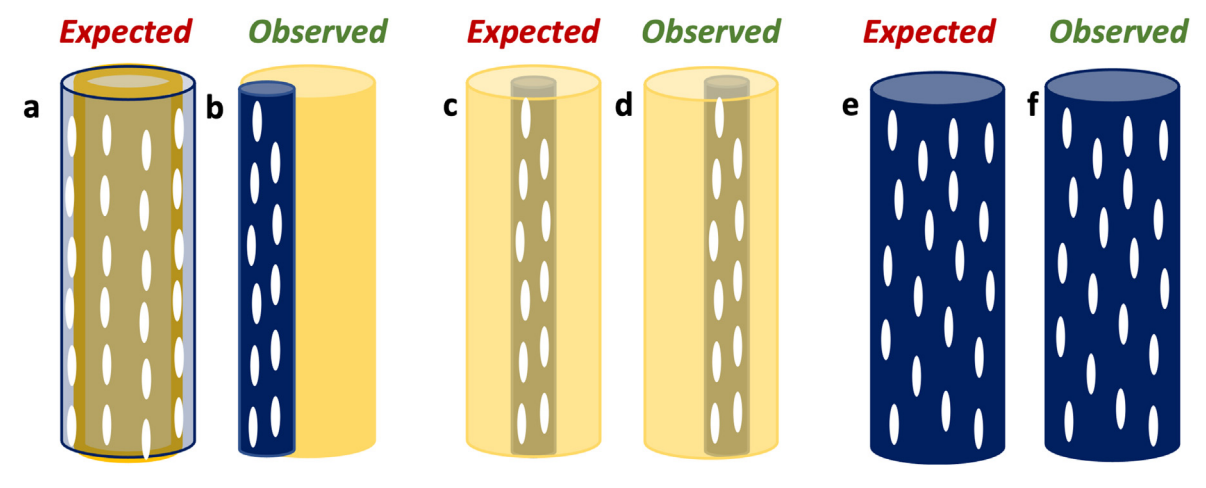


Fig. 6. Schematics of the (a, c, e) expected and (b, d, f) experimentally obtained morphologies of 'BCP sheath' (a—b), 'BCP core' (c—d), and 'BCP both' (e—f), based on SEM images in Figs. 1, 4 and 5.

Table 4Comparison of mechanical properties of polymer fibers.

	'BCP sheath'	'BCP core'	'BCP both'	'PAN both'
Total draw ratio (TDR)	19.8	10.8	13.2	22
Diameter (µm)	13.6	16 ± 3	21 ± 3	12 ± 0.2
Tensile Strength (MPa)	580 ± 50	760 ± 40	570 ± 20	902 ± 19
Tensile Modulus (GPa)	11.0 ± 1	16.8 ± 0.5	10.3 ± 0.3	18.5 ± 0.4
Elongation at Break (%)	5.2 ± 0.6	7.8 ± 0.4	9.7 ± 0.4	7.9 ± 0.9

were comparable. BCP derived fibers used a combination of lower molecular weight PAN (100 kDa in the BCP) and higher molecular PAN (500 kDa) while the blends only used the higher molecular weight PAN (500 kDa). Tuning the molecular weight of the BCP could be one of the potential paths forward to improve the tensile properties of these fibers. Thus, gel-spinning PAN/PMMA-*b*-PAN fibers in a core-sheath cross-sectional geometry provides a

promising means for designing good mechanical property porous carbon fibers.

Variables including the pyrolysis temperature, position of BCP, and the tension during pyrolysis influenced the structural parameters of carbon fibers. Integrated WAXD plots of all porous carbon fibers (Fig. S8) showed typical PAN-derived carbon peaks at ~26° corresponding to (002) and 43° corresponding to (10l) (overlapping 100 and 101) planes. The structural parameters are summarized in Table 7. First, at the carbonization temperature of 1315 °C under tension, 'BCP sheath' and 'BCP core' carbon fibers did not differ significantly in their structural parameters, consistent with their mechanical properties. For bicomponent polymer fibers, the position of BCP affected the orientation of the turbostratic planes after pyrolysis at 800 °C without tension. 'BCP sheath' carbon fibers had no preferential orientation while the 'BCP core' fibers had a modest orientation factor of 0.37. Excluding the orientation factor, their other structural parameters were similar. Second, the application of

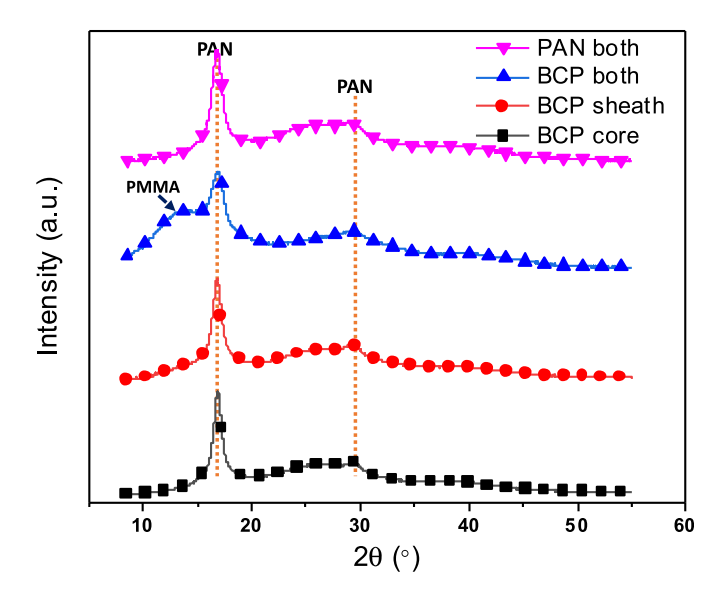


Fig. 7. Integrated WAXD plots of 'BCP both', 'BCP sheath', 'BCP core', and 'PAN both' polymer fibers.

tension during pyrolysis at 800 °C improved the orientation factor of the turbostratic planes from zero to 0.74 and from 0.37 to 0.72 for 'BCP sheath' and "BCP core' carbon fibers, respectively. Lastly, the crystal sizes and orientation factor increased with the

Table 6Mechanical properties of carbon fibers from bicomponent polymer fibers carbonized under tension.^a

	800 °C	1315 °C	
	BCP core	BCP sheath	BCP core
Tensile Strength (GPa) Tensile Modulus (GPa) Elongation at Break (%)	0.3 ± 0.1 70 ± 60 0.4 ± 0.1	1.1 ± 0.3 190 ± 20 0.6 ± 0.1	1.2 ± 0.6 179 ± 17 0.7 ± 0.3

^a 'BCP sheath' carbon fibers after pyrolysis at 800 °C under tension were too brittle and could not be tested for mechanical properties.

carbonization temperature due to a higher degree of turbostratic ordering. Comparing the fibers carbonized under tension, the higher relative intensity of the 43° peak and the lower FWHM of the fibers pyrolyzed at 1315 °C than those at 800 °C corroborated the higher crystallite size (L_{10l}) and mechanical performance.

3.4. Electrochemical energy storage performance

Owing to the mechanical strength and porosity, these carbon fibers have dual functions of structural support and energy storage. To evaluate their capability of storing electrochemical energy, the fibers were tested by cyclic voltammetry (CV) in a three-electrode configuration using a reference electrode of Ag/AgCl. After pyrolysis at 800 °C under no tension, 'BCP sheath' carbon fibers exhibited the highest capacitance of 49 F g $^{-1}$ (Fig. 9). Under tension, however, the capacitance decreased to 19 F g $^{-1}$ and 11 F g $^{-1}$ after pyrolysis at

Table 5Structural properties of polymer fibers.

	BCP sheath TDR 19.8	BCP core TDR 10.8	BCP both TDR 13.2	PAN both TDR 22
Crystallinity (%) ^a	50	54	42	58
Crystal size (nm) ^b	8.9	10.5	6.7	8.4
f_{PAN}^c	0.71	0.75	0.49	0.85
f_{PAN}^{c} $d_{17^{\circ}}/d_{30}^{\circ d}$	1.731	1.731	1.727	1.734

^a Crystallinity is calculated by excluding the amorphous peaks of PAN and BCP from the PAN crystalline peaks (Supplementary Info P1).

 $[^]d$ Ratio of d-spacing of diffraction peaks at 2θ ~17° and ~30°.

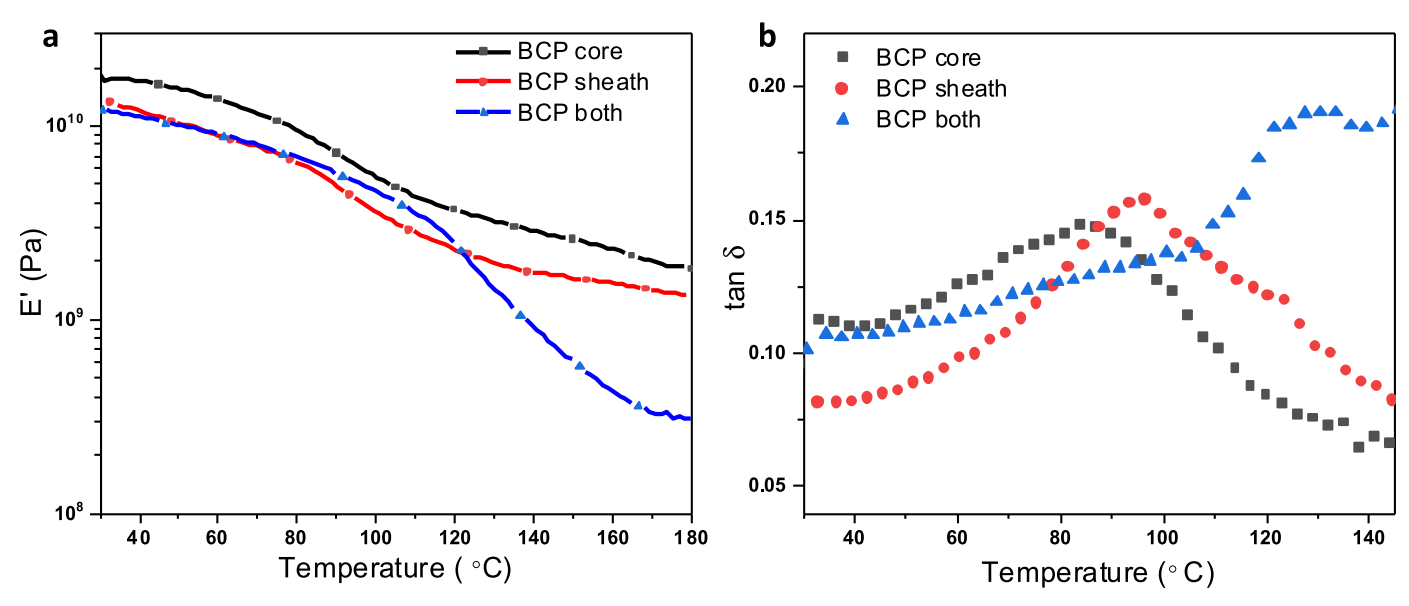


Fig. 8. Dynamic mechanical analysis of 'BCP both', 'BCP sheath', and 'BCP core' polymer fibers at 1 Hz: a) storage modulus and b) tan δ .

^b Crystal size of PAN at $2\theta \sim 17^{\circ}$ (200) and (110) planes.

C Herman's orientation factor of PAN calculated from the azimuthal scan of PAN (200) and (110) planes (and adding the contribution after deconvolution of meridional peak at 78 at 17°)

Table 7Comparison of structural properties of carbon fibers from bicomponent polymer fibers.

Condition	Configuration	L ₀₀₂ (nm) ^a	L _{10l} (nm) ^b	f ₀₀₂ c
800 °C, Tension	BCP sheath	1.33	1.21	0.74
	BCP core	1.65	1.30	0.72
1315 °C, Tension	BCP sheath	1.51	2.11	0.78
	BCP core	1.76	2.70	0.79
800 °C, No tension	BCP sheath	1.23	1.30	0
	BCP core	1.28	1.33	0.37

Crystal size of.

- a (002) plane at $2\theta \sim 26^{\circ}$.
- ^b (10l) plane at $2\theta \sim 43^{\circ}$.
- ^c Orientation factor of (002) plane.

800 and 1315 °C, respectively. Irrespective of the pyrolysis temperature, the application of tension decreased the energy storage capability of the fibers, which could be explained by the decrease in pore accessibility (ion screening, reduced quantum capacitance) with the accompanied increase in turbostractic ordering (Table 7) [47–50]. Further, the lower capacitance of fibers pyrolyzed at 1315 °C under tension was due to decreased pseudocapacitance from elimination of heteroatoms at high pyrolysis temperatures [16]. Specifically, high pyrolysis temperatures remove nitrogen heteroatoms from the carbon electrode, thus reducing the pseudocapacitive contribution to the overall capacitance [15,51,52]. Previous studies in PMMA-b-PAN derived carbon fiber also showed diminishing heteroatomic doping with increasing temperature [16]. Since the fibers in this study are derived from the same type of block copolymer, the rapid loss of capacitance for the 1315 °C carbon fibers in the increasing scan rates (Fig. 9) reflects a fast-kinetic contribution to capacitance which aligns with previous reports on block-copolymer derived porous carbon fibers [15–17,53,54]. Nevertheless, the capacitance of porous carbon fibers from 'BCP sheath' produced under tension at 1315 °C was 4-10 times higher than the commercially produced non-porous carbon fibers including T300 and IM7 (1 F g^{-1} and 3 F g^{-1} , respectively) [55]. Thus, this study has opened potential pathway to satisfy the dual requirements of structural energy storage materials by deriving porous carbon fibers from materials such as gel-spun PMMA-b-PAN precursors.

Considering the capacitance reduction upon tension, we focused on the electrochemical properties of non-tensioned carbon fibers prepared at $800\,^{\circ}$ C. 'BCP both' carbon fibers showed the highest

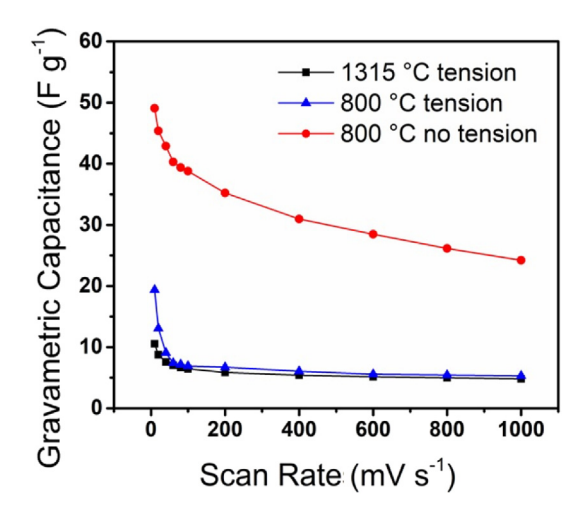


Fig. 9. Capacitive rate capability for 'BCP sheath' carbon fibers after pyrolysis at 1315 and $800 \,^{\circ}\text{C}$ with or without tension.

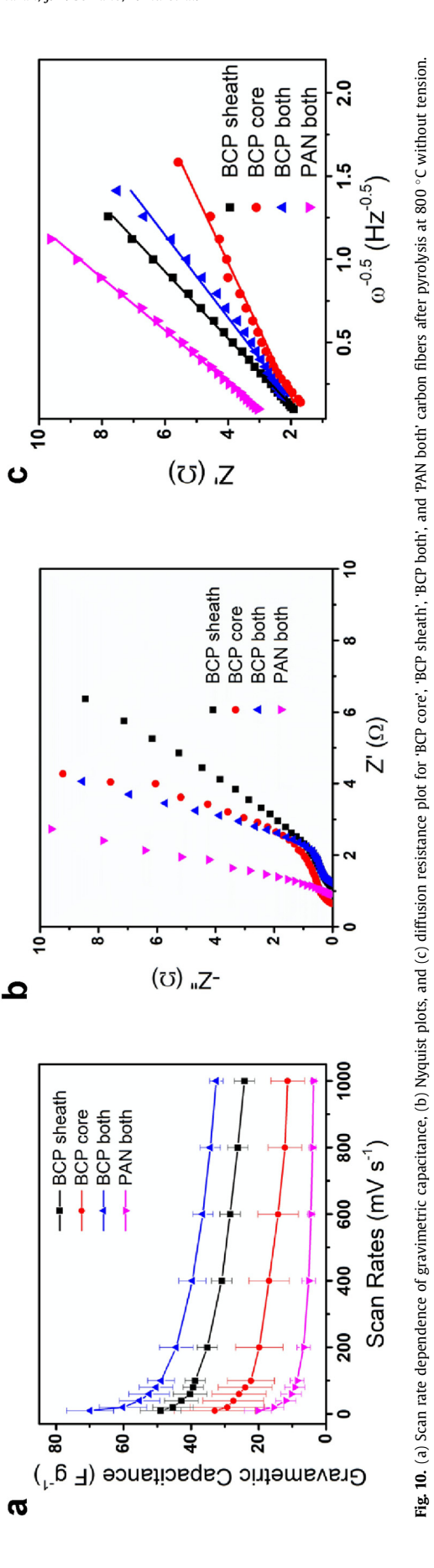
capacitance followed by 'BCP sheath', 'BCP core', and 'PAN both', with gravimetric capacitances of 70, 49, 33, and 20 F g⁻¹ at 10 mV s^{-1} , respectively (Fig. 10a). To evaluate the rate capability, *i.e.*, the capacitance retained at higher charge/discharge rates, the scan rate was tested in the range $10-1000 \text{ mV s}^{-1}$ 'BCP sheath' carbon fibers displayed the highest retention rate (49%), followed by 'BCP both' (46%), 'BCP core' (35%), and 'PAN both' (18%) (Fig. 10a) as the scan rate was increased from 10 to 1000 mV s⁻¹. Based on the Nyquist plot (Fig. 10b) from electrochemical impedance spectroscopy (EIS), combined series resistances (R_s) were all low for 'PAN both' (0.6 Ω), 'BCP core' (0.8 Ω), 'BCP both' (1.2 Ω), and 'BCP sheath' (1.3 Ω) carbon fibers. Using the resistive perturbation of the carbon fibers, the diffusion resistance (σ) (Fig. 10c) was also calculated for 'BCP sheath', 'BCP both', 'BCP core', and 'PAN both' corresponding to 5.3, 3.5, 2.5, and 6.2 Ω s^{-0.5}, respectively.

Within the potential window of 0.0-0.8 V vs. Ag/AgCl in an electrolyte of 3 M KOH, the electrodes were stable, showing no discernible redox peaks [56]. The absence of redox peaks suggests that electrical double layer dominates the energy storage process [57]. 'BCP both' carbon fibers showed the highest capacitance, owing to the largest surface area for adsorbing ions (264 m² g⁻¹) (Fig. 3c). 'BCP sheath' possess the second highest pore surface area (27 m² g⁻¹) and thus second highest capacitance. 'BCP core' follows suit (2 m^2 g^{-1}) and finally 'PAN both', as expected, devoid of mesopores and thus the lowest capacitance. In a previous study, porous carbon fibers from electrospun PMMA-b-PAN reported gravimetric capacitance of 226 F g^{-1} [15]. Factors including, smaller pore size (~11 nm), higher mesopore volume (0.31 cm³ g⁻¹), higher surface area $(503 \text{ m}^2 \text{ g}^{-1})$ and easier pore accessibility of the carbon fibers derived from electrospun BCP than the gel-spun 'BCP both' (~21 nm) are attributed to their higher capacitance. Controlling the above-mentioned factors in carbon fibers derived from gel-spun BCP is required in further studies to improve their electrochemical performance. At this juncture, it is pertinent to note that the electrochemical performance of carbon fibers derived from gelspun PMMA-b-PAN was not evaluated in previous studies to the best of our knowledge, and this work shows promise for further development in future studies.

3.5. Factors influencing pore size

Tailoring the pore size of the carbon fibers is an effective way to balance the mechanical and electrochemical performance of the resultant porous carbon fibers. The pore sizes of carbon fibers produced in this study had a range from 13 to 30 nm, depending on the carbonization temperature and application of tension. While the gel-spinning of 'BCP both' polymer fibers in our study yielded carbon fibers with average pore size of ~25 nm, carbon fibers with average pore size of ~11 nm were derived from electrospun BCP fibers [15]. Another study of carbon film obtained through pyrolysis of BCP (molecular weight 161 kDa) reported pore sizes in the range of 40-50 nm [25]. The pore sizes of these films differed based on either the solvent or temperature used for annealing. Table S1 lists the pore sizes of carbon fibers of a specific molecular weight obtained from the different configurations and conditions. Electrospun carbon fibers of BCP obtained by varying the molecular weight of BCP and the volume fraction of PAN in the BCP, had pore sizes in the range of 10.9–18.6 nm (measured using N₂ physisorption) [17].

In effect, experimental factors including molecular weight and composition of BCP, method of obtaining the porous carbon fibers (electrospinning vs gel-spinning), processing conditions of BCP starting from the initial stages of polymeric fibers to the final steps of carbonization, seem to affect the pore size in the resultant carbon fibers. Pore size of the carbon fibers are driven by kinetically driven processing parameters, in addition to the thermodynamically



driven phase separation between PMMA and PAN blocks. We conducted a computational study to discern the thermodynamic factor (interaction parameter) and subsequently the domain/pore size (characteristic correlation length) of PMMA in the BCP, for comparison with the experimentally observed pore sizes.

3.6. Results of computational study

As shown in Fig. 11, we observed a decreasing $\chi_{i,j}$ with increasing molecular weights, which agrees well with the previous reports [58,59]. For dimers of PMMA-b-PAN, $\chi_{i,j}$ was the highest for the PMMA Iso & PAN Iso pair (1.377) and the lowest for the Syn PMMA & Syn PAN pair (0.363). For trimer of PMMA-b-PAN, we were able to construct the atactic configuration, and the $\chi_{i,j}$ was calculated as 0.677, which fell between PMMA Iso & PAN Syn (0.830) and PMMA Syn & PAN Iso (0.494) pairs. Consequently, different molecular conformations produced different free energy of mixing for PMMA-b-PAN due to different conformational entropies, thus resulting in varied $\chi_{i,j}$ values. Following the calculation of $\chi_{i,j}$ for the trimer Ata PMMA-b-PAN, the extrapolated value for the synthesized BCP with molecular weight ~160 kDa resulted in 0.2932 (Fig. S9).

The phase separation between PMMA and PAN blocks of BCP was simulated using DPD simulation method as observed (Fig. 12a), which agrees with earlier studies [15,60,61]. For the sake of simplicity in the simulations, the kinetic factors involving solvent evaporation effects, crosslinking of PAN during stabilization, thermal shrinkage during pyrolysis, etc., were not considered in the current study. Based on the predicted morphology, the RDF analysis and structure factor S(k) were implemented, which revealed the characteristic correlation length of PMMA-b-PAN to be ~20 nm.

The characteristic correlation length of PMMA-*b*-PAN calculated from DPD simulations is in good agreement with the experimentally determined pore sizes (10–30 nm), which were generated with decomposition of the sacrificial PMMA block. Although, in the experiments in this study, the phase separation of PAN and PMMA blocks may start during their dissolution process in solvent, and the domain size of PMMA could be further altered during the gelspinning process (solvent removal in the coagulation bath, drawing of the polymer precursor fibers, crosslinking of PAN during stabilization, shrinkage accompanying pyrolysis *etc.*), please note that the DPD simulations in this study pursue the thermodynamic

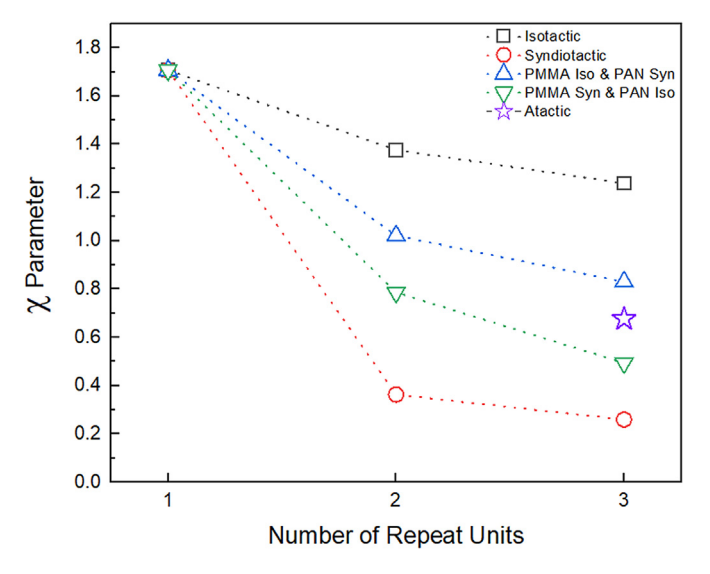


Fig. 11. Calculated $\chi_{i,j}$ parameters with respect to number of repeat units of PMMA and PAN.

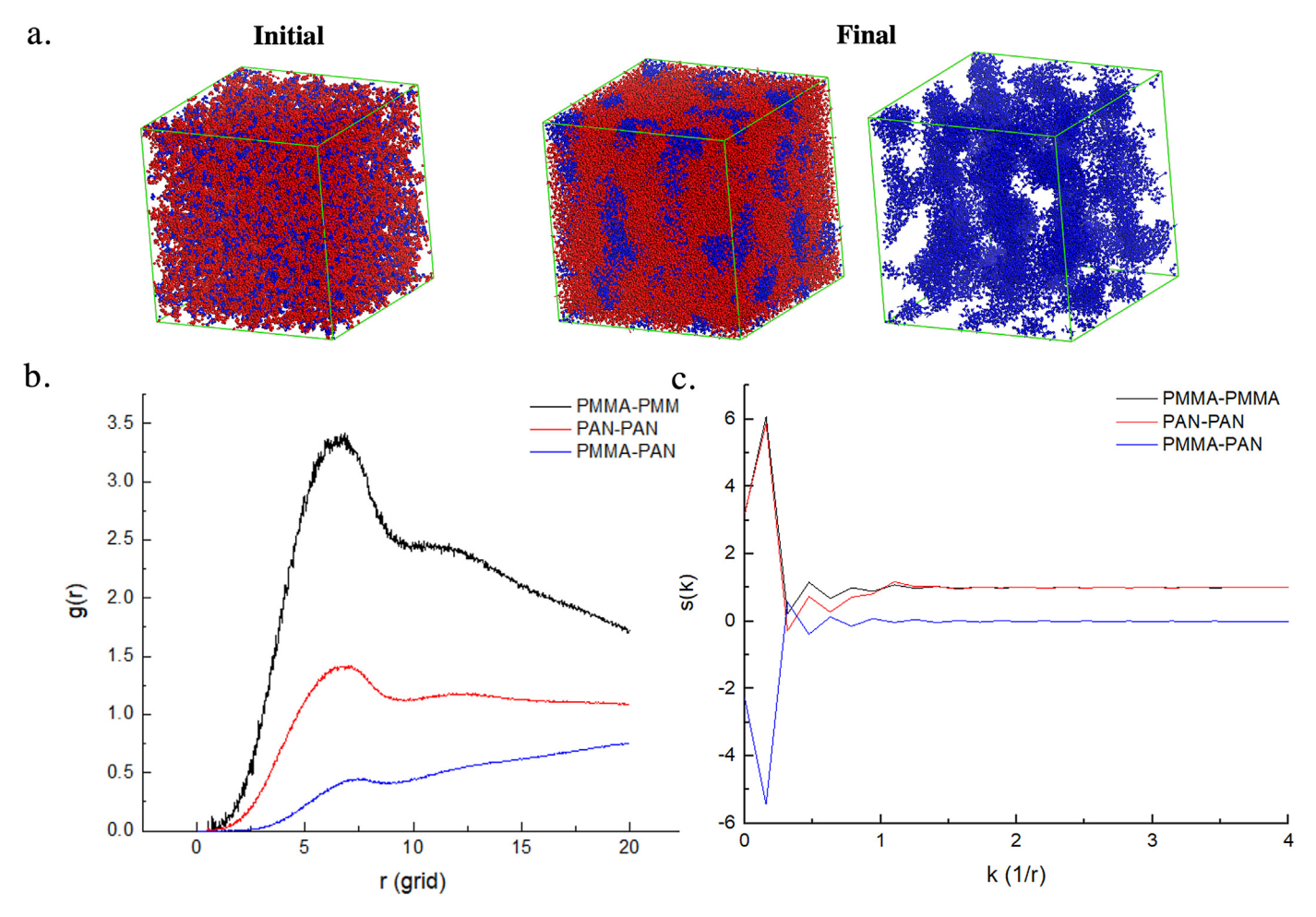


Fig. 12. (a) Initial and final structures of PMMA-b-PAN after phase separation. Red and blue beads denote PMMA and PAN, respectively. For better visualization, PMMA beads were removed, (b) Radial distribution function (RDF) and (c) Structural factor of PMMA-PMMA, PAN-PAN, and PMMA-PAN beads displayed in black, red, and blue line, respectively.

equilibrium for phase separation only, to give an estimate of the pore sizes in the resultant BCP-derived carbon fibers.

4. Conclusion

Herein, we gel-spun four polymer fiber configurations utilizing both PMMA-b-PAN and PAN, including 'BCP sheath', 'BCP core', 'BCP both', and 'PAN both'. By systematically varying the carbonization temperature (800 and 1315 °C) and processing tension (tension and non-tensioned), we elucidated the morphological, mechanical and electrochemical properties of the resultant carbon fibers. Owing to the different rheological properties of PMMA-b-PAN and PAN, and their position in the polymer fibers, they revealed different crosssectional and porous morphologies. Upon pyrolysis without tension, 'BCP sheath' carbon fibers showed a side-by-side morphology with elongated pores confined to a side; 'BCP core' carbon fibers exhibited elongated pores only in the interior encapsulated by nonporous exterior carbon sheath; 'BCP both' carbon fibers displayed well distributed elongated pores both on the interior and exterior; 'PAN both' carbon fibers were non-porous. Without tension, all BCP-containing fibers successfully produced porous carbon fibers after pyrolysis at 800 °C, with an average mesopore size of ~23 nm. Mechanically, 'BCP sheath' fibers showed tensile strength of 1.1 GPa, tensile modulus of 190 GPa, and electrochemical capacitance of 11 F g^{-1} , after pyrolysis at 1315 °C under tension. At a reduced pyrolysis temperature of 800 °C, the electrochemical capacitance

increased slightly from 11 to 19 F g $^{-1}.$ Among the BCP-derived carbon fibers, 'BCP both' carbon fibers after pyrolysis at 800 $^{\circ}\text{C}$ without tension achieved the best capacitance of 70 F g⁻¹ at 10 mV s⁻¹ among all gel-spun carbon fibers. In general, the application of tension and a high pyrolysis temperature improve the mechanical properties but reduce the electrochemical performance of the carbon fibers. Pore size of the carbon fibers are influenced by kinetically driven processing conditions, in addition to the thermodynamic phase separation between PMMA and PAN blocks. Interaction parameter (0.2932) and characteristic correlation length (~20 nm) of BCP, as calculated from thermodynamically governed computational calculation, provide an estimate of the pore sizes observed in the experimentally obtained carbon fibers. Thus, gel-spinning of bicomponent fibers of PMMA-b-PAN and PAN provides an effective means for designing porous carbon fibers with controlled mechanical and electrochemical properties. Tailoring the pore size of BCP-derived carbon fibers by intertwining the thermodynamic and kinetic parameters could be focused on the future studies for balancing their mechanical and electrochemical performance.

CRediT authorship contribution statement

Jyotsna Ramachandran: Conceptualization, Methodology, Investigation, Formal analysis, Project administration, Writing — original draft. **Joel M. Serrano:** Conceptualization, Methodology,

Investigation, Formal analysis, Project administration, Writing — original draft. **Tianyu Liu:** Methodology, Investigation, Formal analysis, Writing — review & editing. **Jinwon Cho:** Methodology, Investigation, Software, Formal analysis, Writing — original draft. **Pedro J. Arias-Monje:** Investigation, Writing — review & editing. **Mingxuan Lu:** Investigation, Writing — review & editing. **Mohammad Hamza Kirmani:** Investigation, Writing — review & editing. **Seung Soon Jang:** Conceptualization, Supervision, Writing — review & editing. **Guoliang Liu:** Conceptualization, Funding acquisition, Supervision, Writing — review & editing. **Satish Kumar:** Conceptualization, Funding acquisition, Supervision, Writing — review & editing.

Declaration of competing interest

The authors declare that they have no known competing financial interests or personal relationships that could have appeared to influence the work reported in this paper.

Acknowledgment

This material is based upon work supported by the Air Force Office of Scientific Research under award number FA9550-17-1-0112 through the Young Investigator Program (YIP) and FA9550-14-1-0194. This work was partially supported by the National Science Foundation award number DMR-1752611. Pedro J. Arias-Monje is supported by a Fulbright-Colciencias fellowship. We acknowledge the use of the Nanoscale Characterization and Fabrication Laboratory (NCFL) and chemistry facilities at Virginia Tech and the Georgia Tech Institute for Electronics and Nanotechnology, a member of the National Nanotechnology Coordinated Infrastructure (NNCI), which is supported by the National Science Foundation (ECCS-2025462).

Appendix A. Supplementary data

Supplementary data to this article can be found online at https://doi.org/10.1016/j.carbon.2022.02.044.

References

- [1] S. Chen, L. Qiu, H.M. Cheng, Carbon-based fibers for advanced electrochemical energy storage devices, Chem. Rev. 120 (5) (2020) 2811–2878, https://doi.org/ 10.1021/acs.chemrev.9b00466.
- [2] B.A. Newcomb, Processing, structure, and properties of carbon fibers, Compos. Appl. Sci. Manuf. (2016), https://doi.org/10.1016/j.compositesa.2016.10.018.
- [3] B.A. Newcomb, H.G. Chae, The properties of carbon fibers, in: Handbook of Properties of Textile and Technical Fibres, Woodhead Publishing, 2018, pp. 841–871, https://doi.org/10.1016/b978-0-08-101272-7.00021-3.
- [4] Y. Chen, A. Amiri, J.G. Boyd, M. Naraghi, Promising trade-offs between energy storage and load bearing in carbon nanofibers as structural energy storage devices, Adv. Funct. Mater. 29 (33) (2019) 1–11, https://doi.org/10.1002/ adfm.201901425.
- [5] H. Qian, H. Diao, N. Shirshova, E.S. Greenhalgh, J.G.H. Steinke, M.S.P. Shaffer, A. Bismarck, Activation of structural carbon fibres for potential applications in multifunctional structural supercapacitors, J. Colloid Interface Sci. 395 (1) (2013) 241–248, https://doi.org/10.1016/j.jcis.2012.12.015.
- [6] L.E. Asp, E.S. Greenhalgh, Structural power composites, Compos. Sci. Technol. 101 (2014) 41–61, https://doi.org/10.1016/j.compscitech.2014.06.020.
- [7] N. Shirshova, H. Qian, M.S.P. Shaffer, J.H.G. Steinke, E.S. Greenhalgh, P.T. Curtis, A. Kucernak, A. Bismarck, Structural composite supercapacitors, Composer Part A Appl. Sci. Manuf. 46 (2013) 96–107, https://doi.org/10.1016/ j.compositesa.2012.10.007.
- [8] W. Johannisson, N. Ihrner, D. Zenkert, M. Johansson, D. Carlstedt, L.E. Asp, F. Sieland, Multifunctional performance of a carbon fiber UD lamina electrode for structural batteries, Compos. Sci. Technol. 168 (August) (2018) 81–87, https://doi.org/10.1016/j.compscitech.2018.08.044.
- [9] W. Johannisson, D. Zenkert, G. Lindbergh, Model of a structural battery and its potential for system level mass savings, Multifunct. Mater. 2 (3) (2019), 035002, https://doi.org/10.1088/2399-7532/ab3bdd.
- [10] L.E. Asp, M. Johansson, G. Lindbergh, J. Xu, D. Zenkert, Structural battery composites: a review, Funct. Compos. Struct. 1 (4) (2019), 042001, https://

- doi.org/10.1088/2631-6331/ab5571.
- [11] N. Shirshova, H. Qian, M. Houllé, J.H.G. Steinke, A.R.J. Kucernak, Q.P.V. Fontana, E.S. Greenhalgh, A. Bismarck, M.S.P. Shaffer, Multifunctional structural energy storage composite supercapacitors, Faraday Discuss 172 (2014) 81–103, https://doi.org/10.1039/c4fd00055b (0).
- [12] Y. Chen, J. Cai, J.G. Boyd, W.J. Kennedy, M. Naraghi, Mechanics of emulsion electrospun porous carbon fibers as building blocks of multifunctional materials, ACS Appl. Mater. Interfaces 10 (44) (2018) 38310–38318, https:// doi.org/10.1021/acsami.8b10499.
- [13] E. Jo, J.G. Yeo, D.K. Kim, J.S. Oh, C.K. Hong, Preparation of well-controlled porous carbon nanofiber materials by varying the compatibility of polymer blends, Polym. Int. 63 (8) (2014) 1471–1477, https://doi.org/10.1002/pi.4645.
- [14] C. Kim, Y. Il Jeong, B.T.N. Ngoc, K.S. Yang, M. Kojima, Y.A. Kim, M. Endo, J.W. Lee, Synthesis and characterization of porous carbon nanofibers with hollow cores through the thermal treatment of electrospun copolymeric nanofiber webs, Small 3 (1) (2007) 91–95, https://doi.org/10.1002/smll.200600243.
- [15] Z. Zhou, T. Liu, A.U. Khan, G. Liu, Block copolymer—based porous carbon fibers, Sci. Adv. 5 (2) (2019) eaau6852, https://doi.org/10.1126/sciadv.aau6852.
- [16] Z. Zhou, T. Liu, A.U. Khan, G. Liu, Controlling the physical and electrochemical properties of block copolymer-based porous carbon fibers by pyrolysis temperature, Mol. Syst. Des. Eng. 5 (1) (2020) 153–165, https://doi.org/10.1039/ c9me00066f.
- [17] J.M. Serrano, T. Liu, A.U. Khan, B. Botset, B.J. Stovall, Z. Xu, D. Guo, K. Cao, X. Hao, S. Cheng, G. Liu, Composition design of block copolymers for porous carbon fibers, Chem. Mater. 31 (21) (2019) 8898–8907, https://doi.org/10.1021/acs.chemmater.9b02918.
- [18] T. Liu, G. Liu, Block copolymers for supercapacitors, dielectric capacitors and batteries, J. Phys. Condens. Matter (2019), https://doi.org/10.1088/1361-648X/ ab0d77. IOP Publishing.
- [19] H.G. Chae, B.A. Newcomb, P.V. Gulgunje, Y. Liu, K.K. Gupta, M.G. Kamath, K.M. Lyons, S. Ghoshal, C. Pramanik, L. Giannuzzi, K. Şahin, I. Chasiotis, S. Kumar, High strength and high modulus carbon fibers, Carbon N. Y. 93 (2015) 81–87, https://doi.org/10.1016/j.carbon.2015.05.016.
- [20] Y. Liu, H.G. Chae, Y.H. Choi, S. Kumar, Preparation of low density hollow carbon fibers by Bi-component gel-spinning method, J. Mater. Sci. 50 (10) (2015) 3614–3621, https://doi.org/10.1007/s10853-015-8922-3.
- (2015) 3614–3621, https://doi.org/10.1007/s10853-015-8922-3.
 [21] P.V. Gulgunje, B.A. Newcomb, K. Gupta, H.G. Chae, T.K. Tsotsis, S. Kumar, Lowdensity and high-modulus carbon fibers from polyacrylonitrile with honeycomb structure, Carbon N. Y. 95 (2015) 710–714, https://doi.org/10.1016/i.carbon.2015.08.097.
- [22] N. Shirolkar, A. Maffe, E. DiLoreto, P.J. Arias-Monje, M. Lu, J. Ramachandran, P. Gulgunje, K. Gupta, J.G. Park, K.C. Shih, M.H. Kirmani, A. Sharits, D. Nepal, M.P. Nieh, R. Liang, T. Tsotsis, S. Kumar, Multichannel hollow carbon fibers: processing, structure, and properties, Carbon N. Y. 174 (2021) 730–740, https://doi.org/10.1016/j.carbon.2020.11.077.
- [23] J. Ramachandran, M. Lu, P.J. Arias-Monje, M.H. Kirmani, N. Shirolkar, S. Kumar, Towards designing strong porous carbon fibers through gel spinning of polymer blends, Carbon N. Y. 173 (2021) 724–735, https://doi.org/10.1016/ icarbon.2020.10.029.
- [24] C. González, J.J. Vilatela, J.M. Molina-Aldareguía, C.S. Lopes, J. LLorca, Structural composites for multifunctional applications: current challenges and future trends, Prog. Mater. Sci. 89 (2017) 194–251, https://doi.org/10.1016/ j.pmatsci.2017.04.005.
- [25] Z. Zhou, G. Liu, Controlling the pore size of mesoporous carbon thin films through thermal and solvent annealing, Small 13 (15) (2017) 19–21, https:// doi.org/10.1002/smll.201603107.
- [26] H.C. Liu, J. Luo, H. Chang, A.A. Bakhtiary Davijani, P.-H. Wang, S. Kumar, Polyacrylonitrile sheath and polyacrylonitrile/lignin core Bi-component carbon fiber, Carbon N. Y. 149 (2019) 165–172, https://doi.org/10.1016/ j.carbon.2019.04.004.
- [27] E. Ahmed, C.T. Womble, J. Cho, K. Dancel-Manning, W.J. Rice, S.S. Jang, M. Weck, One-pot synthesis of linear triblock terpolymers and their aqueous self-assembly, Polym. Chem. 12 (13) (2021) 1967–1974, https://doi.org/10.1039/d1py00054c.
- [28] J. Li, S. Wu, C. Wu, L. Qiu, G. Zhu, C. Cui, Y. Liu, W. Hou, Y. Wang, L. Zhang, I. Teng, H.-H. Yang, W. Tan, Versatile surface engineering of porous nanomaterials with bioinspired polyphenol coatings for targeted and controlled drug delivery, Nanoscale 8 (16) (2016) 8600–8606, https://doi.org/10.1039/C6NR006004
- [29] C.P. Callaway, K. Hendrickson, N. Bond, S.M. Lee, P. Sood, S.S. Jang, Molecular modeling approach to determine the flory-huggins interaction parameter for polymer miscibility analysis, ChemPhysChem 19 (13) (2018) 1655–1664, https://doi.org/10.1002/cphc.201701337.
- [30] M. Thommes, K. Kaneko, A.V. Neimark, J.P. Olivier, F. Rodriguez-Reinoso, J. Rouquerol, K.S.W. Sing, Physisorption of gases, with special reference to the evaluation of surface area and pore size distribution (IUPAC technical report), Pure Appl. Chem. 87 (9–10) (2015) 1051–1069, https://doi.org/10.1515/pac-2014-1117.
- [31] M. Naeimirad, A. Zadhoush, R. Kotek, R. Esmaeely Neisiany, S. Nouri Khorasani, S. Ramakrishna, Recent advances in core/shell bicomponent fibers and nanofibers: a review, J. Appl. Polym. Sci. 135 (21) (2018) 28–30, https://doi.org/10.1002/app.46265.
- [32] M. Maqsood, G. Seide, Novel bicomponent functional fibers with sheath/core configuration containing intumescent flame-retardants for textile

- applications, Materials 12 (19) (2019), https://doi.org/10.3390/ma12193095.
- [33] N. Minagawao, J.L. White, Influence of viscosity and die cross-section on interface shape, Engineering 15 (1975) 825–830.
- [34] S.P. Rwei, Y.T. Lin, Y.Y. Su, Study of self-crimp polyester fibers, Polym. Eng. Sci. 45 (6) (2005) 838–845, https://doi.org/10.1002/pen.20338.
- [35] C. Prahsarn, W. Klinsukhon, N. Roungpaisan, N. Srisawat, Self-crimped bicomponent fibers containing polypropylene/ethylene octene copolymer, Mater. Lett. 91 (2013) 232–234, https://doi.org/10.1016/j.matlet.2012.09.106.
- [36] T.H. Oh, Effects of spinning and drawing conditions on the crimp contraction of side-by-side poly(trimethylene terephthalate) bicomponent fibers, J. Appl. Polym. Sci. 102 (2) (2006) 1322–1327, https://doi.org/10.1002/app.23988.
- [37] T. Lin, H. Wang, X. Wang, Self-crimping bicomponent nanofibers electrospun from polyacrylonitrile and elastomeric polyurethane, Adv. Mater. 17 (22) (2005) 2699–2703. https://doi.org/10.1002/adma.200500901.
- [38] A.T. Chien, P.V. Gulgunje, H.G. Chae, A.S. Joshi, J. Moon, B. Feng, G.P. Peterson, S. Kumar, Functional polymer-polymer/carbon nanotube Bi-component fibers, Polymer 54 (22) (2013) 6210–6217, https://doi.org/10.1016/ j.polymer.2013.08.061.
- [39] J. Wiley, Effect of Crimp on the Tensile and Compressive Properties, No. I, 1971, pp. 1539–1544.
- [40] H.C. Liu, A.T. Chien, B.A. Newcomb, Y. Liu, S. Kumar, Processing, structure, and properties of lignin- and CNT-incorporated polyacrylonitrile-based carbon fibers, ACS Sustain. Chem. Eng. 3 (9) (2015) 1943–1954, https://doi.org/ 10.1021/acssuschemeng.5b00562.
- [41] H.G. Chae, M.L. Minus, S. Kumar, Oriented and exfoliated single wall carbon nanotubes in polyacrylonitrile, Polymer 47 (10) (2006) 3494–3504, https:// doi.org/10.1016/j.polymer.2006.03.050.
- [42] D. Sawai, T. Kanamoto, H. Yamazaki, K. Hisatani, Dynamic mechanical relaxations in poly(acrylonitrile) with different stereoregularities, Macromolecules 37 (8) (2004) 2839–2846, https://doi.org/10.1021/ma0352330.
- [43] A.T. Chien, B.A. Newcomb, D. Sabo, J. Robbins, Z.J. Zhang, S. Kumar, High-strength superparamagnetic composite fibers, Polymer 55 (16) (2014) 4116–4124, https://doi.org/10.1016/j.polymer.2014.06.028.
- [44] H. Chang, J. Luo, H.C. Liu, A.A. Bakhtiary Davijani, P.H. Wang, G.S. Lolov, R.M. Dwyer, S. Kumar, Ductile polyacrylonitrile fibers with high cellulose nanocrystals loading, Polymer 122 (2017) 332–339, https://doi.org/10.1016/ i.polymer.2017.06.072.
- [45] B. Lu, K. Lamnawar, A. Maazouz, H. Zhang, Revealing the dynamic heterogeneity of PMMA/PVDF blends: from microscopic dynamics to macroscopic properties, Soft Matter 12 (13) (2016) 3252–3264, https://doi.org/10.1039/c5sm02659h.
- [46] S. Lee, J. Kim, B.-C. Ku, J. Kim, H.-I. Joh, Structural evolution of polyacrylonitrile fibers in stabilization and carbonization, Adv. Chem. Eng. Sci. (2012) 275–282, https://doi.org/10.4236/aces.2012.22032, 02 (02).
- [47] H. Ji, X. Zhao, Z. Qiao, J. Jung, Y. Zhu, Y. Lu, L.L. Zhang, A.H. MacDonald, R.S. Ruoff, Capacitance of carbon-based electrical double-layer capacitors, Nat. Commun. 5 (Cmcm) (2014), https://doi.org/10.1038/ncomms4317.
- [48] B. Dyatkin, Y. Gogotsi, Effects of structural disorder and surface chemistry on electric conductivity and capacitance of porous carbon electrodes, Faraday Discuss 172 (2014) 139–162, https://doi.org/10.1039/c4fd00048j.
- [49] B.S. Lee, S.B. Son, K.M. Park, W.R. Yu, K.H. Oh, S.H. Lee, Anodic properties of hollow carbon nanofibers for Li-ion battery, J. Power Sources 199 (2012)

- 53-60, https://doi.org/10.1016/j.jpowsour.2011.10.030.
- [50] G. Fredi, S. Jeschke, A. Boulaoued, J. Wallenstein, M. Rashidi, F. Liu, R. Harnden, D. Zenkert, J. Hagberg, G. Lindbergh, P. Johansson, L. Stievano, L.E. Asp, Graphitic microstructure and performance of carbon fibre Li-ion structural battery electrodes, Multifunct. Mater. 1 (1) (2018), https://doi.org/10.1088/ 2399-7532/aab707.
- [51] Z. Zhang, Y. Zhang, X. Mu, J. Du, H. Wang, B. Huang, J. Zhou, X. Pan, E. Xie, The carbonization temperature effect on the electrochemical performance of nitrogen-doped carbon monoliths, Electrochim. Acta 242 (2017) 100–106, https://doi.org/10.1016/j.electacta.2017.05.016.
- [52] B. Xu, F. Wu, S. Chen, Z. Zhou, G. Cao, Y. Yang, High-capacitance carbon electrode prepared by PVDC carbonization for aqueous EDLCs, Electrochim. Acta 54 (8) (2009) 2185–2189, https://doi.org/10.1016/ i.electacta.2008.10.032.
- [53] M. Zhong, E.K. Kim, J.P. McGann, S.E. Chun, J.F. Whitacre, M. Jaroniec, K. Matyjaszewski, T. Kowalewski, Electrochemically active nitrogen-enriched nanocarbons with well-defined morphology synthesized by pyrolysis of selfassembled block copolymer, J. Am. Chem. Soc. 134 (36) (2012) 14846–14857, https://doi.org/10.1021/ja304352n.
- [54] T. Liu, Z. Zhou, Y. Guo, D. Guo, G. Liu, Block copolymer derived uniform mesopores enable ultrafast electron and ion transport at high mass loadings, Nat. Commun. 10 (1) (2019) 1–10, https://doi.org/10.1038/s41467-019-08644-w.
- [55] J.F. Snyder, E.L. Wong, C.W. Hubbard, Evaluation of commercially available carbon fibers, fabrics, and papers for potential use in multifunctional energy storage applications, J. Electrochem. Soc. 156 (3) (2009) A215, https://doi.org/ 10.1149/1.3065070.
- [56] G. He, Y. Song, S. Chen, L. Wang, Porous carbon nanofiber mats from electrospun polyacrylonitrile/polymethylmethacrylate composite nanofibers for supercapacitor electrode materials, J. Mater. Sci. 53 (13) (2018) 9721–9730, https://doi.org/10.1007/s10853-018-2277-5.
- [57] V. Khomenko, E. Raymundo-Piñero, F. Béguin, Optimisation of an asymmetric manganese oxide/activated carbon capacitor working at 2 v in aqueous medium, J. Power Sources 153 (1) (2006) 183–190, https://doi.org/10.1016/ j.jpowsour.2005.03.210.
- [58] V.A. Gracia-Medrano-Bravo, L. Merklein, N. Oberle, M. Batora, P. Scharfer, W. Schabel, Determination of binary interaction parameters for ternary polymer-polymer-solvent systems using Raman spectroscopy, Adv. Mater. Technol. 6 (2) (2021) 1–8, https://doi.org/10.1002/admt.202000149.
- [59] T. Kyu, R.A. Matkar, D.S. Lim, C. Ko, Discrepancy in determination of χ parameters by melting point depression versus small-angle neutron scattering in blends of deuterated polycarbonate and isotactic poly(methyl methacrylate), J. Appl. Crystallogr. 40 (SUPPL. 1) (2007) 675–679, https://doi.org/10.1107/S0021889806054999.
- [60] C.T. Nguyen, D.P. Kim, Direct preparation of mesoporous carbon by pyrolysis of poly(acrylonitrile-b-methylmethacrylate) diblock copolymer, J. Mater. Chem. 21 (37) (2011) 14226–14230, https://doi.org/10.1039/c1jm10920k.
- [61] T. Uemura, T. Kaseda, Y. Sasaki, M. Inukai, T. Toriyama, A. Takahara, H. Jinnai, S. Kitagawa, Mixing of immiscible polymers using nanoporous coordination templates, Nat. Commun. 6 (May) (2015), https://doi.org/10.1038/ ncomms8473.